Nanoscale

Polymer-Metal Coating for high contrast SEM cross sections at the deep nanoscale

Journal:	*Nanoscale*
Manuscript ID	NR-ART-08-2018-006669.R1
Article Type:	Paper
Date Submitted by the Author:	08-Nov-2018
Complete List of Authors:	Staaks, Daniel; E O Lawrence Berkeley National Laboratory, The Molecular Foundry; Ilmenau University of Technology, Dept. of Micro- and Nanoelectronic Systems Olynick, Deirdre; University of California San Francisco Rangelow, Ivo; Ilmenau University of Technology, Dept. of Micro- and Nanoelectronic Systems Altoe, Virginia; Lawrence Berkeley National Laboratory, The Molecular Foundry

Journal Name

ARTICLE

Polymer-Metal Coating for high contrast SEM cross sections at the deep nanoscale

eceived 00th January 20xx,
Accepted 00th January 20xx

DOI: 10.1039/x0xx00000x

www.rsc.org/

D. Staaks[a,b], D. L. Olynick[a], I. W. Rangelow[b], and M. V. P. Altoe[a]

In scanning electron microscopy (SEM), imaging nanoscale features by means of the cross-sectioning method becomes increasingly challenging with shrinking feature sizes. However, obtaining high quality images, at high magnification, is crucial for critical dimension and patterned feature evaluation. Therefore, in this work, we present a new sample preparation method for high performance cross-sectional secondary electron (SE) imaging, targeting features at the deep nanoscale and into the sub-10 nm regime. Different coating architectures including conductive and non-conductive polymer, carbon and metal are compared on their ability to discern etching feature profiles and materials interfaces of densely packed nano-patterned features. A stacked coating of polymer and metal produced better visibility mainly due to enhancement of contrast between feature and background. Contrast was evaluated by using histograms of intensity of gray levels directly derived from SE images, obtained by the SE in-lens detector. In polymer-metal coatings (PMC), optimization of contrast is explored by varying the thickness of the metal layer and results are discussed in terms of the effectiveness of the metal layer in reducing the escape of secondary electrons (SE) generated in the polymer layer and feature. Other advantages of PMCs are their cleanroom compatibility and ease of coating removal.

Introduction

Scanning electron microscopy is one of the most powerful methods of inspection and metrology in micro- and nanotechnologies. It has been an established “workhorse” in research as well as industrial environments for more than half a century[1,2]. A well known method in SEM for obtaining information about the vertical dimension of a sample and its interfaces is cross-sectioning, a technique in which the sample is cleaved and mounted in a way so that it can be viewed at an angle of up to 90° relative to its top surface (the plane of the wafer). This is ideal for imaging lithography and etching profiles which are hidden when the sample is viewed from the top of the wafer. There are numerous publications available for top down scanning electron microscopy (TD SEM), explaining how to optimize sample preparation and imaging conditions for improving contrast and resolution[3–6]. On the other hand, a comprehensive discussion of methods for attaining high quality cross-sectional SEM (CS SEM) images aimed to non-conductive densely packed nano-patterned features with resolution in the single-digit regime (SDR), to our knowledge, has not been published.

The need for new methods that improve CS SEM becomes clear when looking at lithographic patterning and pattern transfer for nano devices, where feature sizes have been pushing towards smaller dimensions[7,8], and are now entering the single-digit nano regime. For instance, in 2024 the International Roadmap for Semiconductors (ITRS 2.0) is predicting 12 nm minimum metal pitch for micro processing units in the corresponding 2.5 nm technology node[9]. Furthermore, hard disk drive industry anticipates 10 Tb/in² in 2025; requiring 5 nm features for heated-dot magnetic recording (HDMR)[10]. As a consequence, new methods for single-digit pattern generation and pattern transfer are being developed, such as top-down methods like scanning probe lithography (SPL)[11,12], nanoimprint lithography[13], extreme UV (EUV) lithography[14], or bottom-up methods like self aligned block copolymer lithography[15–18] with double patterning[19]. For these reasons, inspection and metrology in scanning electron microscopy for quantitative or qualitative sample information is gradually moving to higher resolutions. Therefore new ways to address these challenges have to be found for academic and industrial SEM metrology[20].

Our initial motivation to investigate new methods to improve CS SEM arose from the need to fabricate bit pattern media[6,21] imprint templates where a layer stack is etched into quartz. To optimize the many steps of the process, samples are fabricated first on silicon dioxide grown on silicon. Reliable, high-throughput, and high contrast imaging of single-digit features in cross sections at each step of the patterning process was a prerequisite for process control of nanometer plasma pattern

[a] Molecular Foundry, Lawrence Berkeley National Laboratory, Berkeley, 94720, United States
[b] Ilmenau Univ. of Technology, Dept. of Micro- and Nanoelectronic Systems, 98684, Germany
Electronic Supplementary Information (ESI) available:
See DOI: 10.1039/x0xx00000x

transfer. High resolution and high contrast CS SEM are especially desired to reveal etched profile shapes, including undercut, notching, bowing, faceting, aspect ratio dependent etching, etch depth, sidewall angle, undercut, mask erosion and residual layer thickness[22]. It can also provide information about the location of a material interface; for example, a silicon/metal interface cross sectioned after a plasma pattern transfer. Undoubtedly, CS SEM of densely packed nano-scale patterned features on non-conductive silicon dioxide substrates are substantially more difficult than of an isolated feature on conductive substrate. In fact, CS SEM of patterned sub-10 nm silicon nanowires without any coating has been reported[23]. However, Ze-Jun et al.[24] have simulated that improvements in contrast and/or signal-to noise ratio can improve edge-to-edge resolution even beyond the theoretical resolution.

Other methods for extraction of sample structure metrology information like 3D image analysis in top down SEM images[25], or stereo SEM[3,26] have been shown, but are heavily limited as they cannot image significantly undercut features. Transmission electron microscopy, can reach atomic resolution and provides good material contrast[27], but is not practical for quick process control, as it requires difficult and time consuming sample preparation, e.g. microtomy or focused ion beam cutting.

Critical dimension scanning electron microscopy (CD SEM)[28], typically a top down imaging method, can also benefit from improved cross-sectional imaging. Better CS SEM can support industrial CD SEM optimization; especially with the increasing need for higher resolution and smaller tolerances[20]. Factors affecting CD SEM, like noise and resolution[29], are also important in CS SEM, where, for example, they can aid in edge detection metrology software for computerized analysis.

In this paper, we present a new sample preparation technique for improving cross-sectional SEM images which greatly enhances the feature to background contrast and allows for imaging nanoscale features at high resolution. We demonstrate that depositing a stack of polymer and metal prior to sample cross-sectioning, strongly enhances contrast between features and background. In addition, we show how to optimize the polymer/metal stack and compare the performance of the stack to more commonly used coatings such as sputtered Au/Pd and sputtered carbon. Through a thorough understanding of CS SEM imaging formation including generation, escape, collection and processing of secondary electrons, we propose a mechanism able to explain the observed increase of contrast based on the role of the metal layer in attenuating secondary electron emission through the top surface. We find several advantages to the polymer metal stack including better ability to discern etching feature profiles and material interfaces, cleanroom compatibility, as well as removability via lift-off.

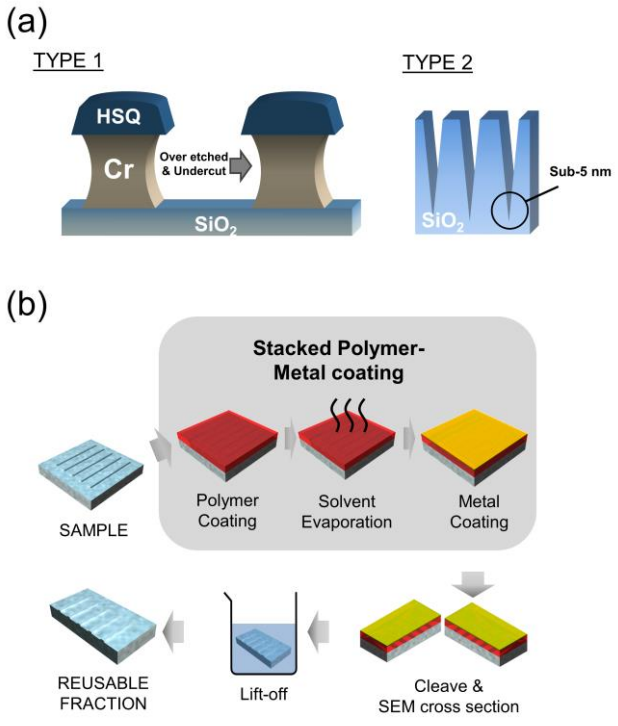

Figure 1: (a) Schematic of sample types used in experiments. Type 1: HSQ masked chromium (over etched) on SiO_2; 60 nm and 200 nm pitch. Type 2: SiO_2 with fingerprint pattern (30 nm pitch) derived from block copolymer lithography and etching. Trench bottom is sub-5 nm wide **(b)** Illustration of polymer-metal coating process steps.

Materials, methods and definitions

Sample Preparation

Sample type 1 (*Figure **1**a left*): Patterned hydrogen silsesquioxane (HSQ) on etched chromium SiO_2 substrate. Starting with a 4" silicon wafer coated with 250 nm (±5 %) dry thermal oxide, chromium was deposited by e-beam evaporation (Semicore SC600) with a 2 Å/s deposition rate to obtain thin chromium films of 20 nm (±1.5 nm) thickness. Substrates were then spin coated with HSQ, which was exposed via e-beam lithography using a Vistec VB300 with acceleration voltage of 100 keV. Resist development was done using 1% NaOH, 4% NaCl. Chromium was etched using an inductively coupled plasma (ICP) etcher (Oxford Plasmalab 150). Process conditions and etch time were chosen to obtain a prominent over etched and undercut profile shape, using a Cl_2/O_2 gas mixture at -50 °C at low oxygen concentration[30].

Sample type 2 (*Figure **1**a right*): Tapered SiO_2 profile with 15 nm trench width and 52 nm etch depth. The initial layer stack (provided by courtesy of Seagate Technology) consisted of a silicon substrate with 300 nm thermal silicon dioxide, 10 nm chromium, and a 30 nm pitch HSQ pattern, derived from unguided block copolymer. After pattern transfer of the HSQ mask into the chromium, silicon dioxide was etched in an ICP etcher using a SF_6/O_2 gas mixture at 20°C. Subsequently, chromium was removed using Cl_2/O_2 ICP plasma etching. The tapered profile allows for bottom trench width of sub–5 nm.

Sample coating

Carbon Coating: Carbon was deposited thermally using pointed carbon rods in a Denton Vacuum Desk V with carbon accessory. Before deposition, the chamber was pumped down to 45 mTorr.

Metal Sputter Coating: Using a Denton Vacuum Desk V, gold-palladium alloy was sputter-coated with current set point at 30 mA and starting chamber pressure of 80 mTorr.

Polymer-metal coating (PMC): The process for polymer-metal coating in CS SEM is illustrated in *Figure* 1*b* and consists of depositing a layer of polymer followed by a layer of metal coating, cleaving, imaging and an optional lift-off.
Two different polymers were used for this work: (1) conventional poly(methyl methacrylate) (PMMA) and (2) a conductive polyaniline compound, AquaSAVE, (from Mitsubishi Rayon Co.) formed from a water dispersed poly(anilinesulfonic acid). For consistency in the experiments, the sample was heated to 150°C in an oven for 5 min in order to reduce moisture on the surface, prior to applying the polymer coating. Polymer coating was done by spin coating (Brewer CEE 100FX) either PMMA $(M_w = 495k)$ in anisole or Aquasave 53ZA (solvent: water). For further information and Spin speed curves for Aquasave see *Sup. A.*
After spin coating, solvent evaporation was achieved by 5 minute bake in an oven at 150°C for Aquasave and 5 min at 180°C for PMMA. Note that we compared conductive polymer-metal coating (CPM) with hard bake temperatures of 100°C, 150°C and 180°C and found no differences in image quality or contrast. Subsequently, samples were coated with Gold/Palladium films as described under "Metal Sputter Coating".
Note that Aquasave shrinks upon imaging by about 20% of its original value (*Sup.* ***A****)*. PMMA shrinks more than 75% upon imaging and it becomes more uneven. Thicker initial coats are therefore required to obtain final thickness that covered the features.

Sample cleaving

Methods for cleaving include manual cleaving of crystalline substrates with a diamond scribe or by using scribe-based cleaving tools[31]. These tools are typically affixed to a microscope to promote more accurate placement of the scribe. For more accuracy, lithography and deep plasma etching[32] or focused ion beam milling can be used[33,34]. Here we use a homemade micrometer cleaving tool to cleave an e-beam exposed pattern of 600 µm long lines. The chip-based samples were cleaved in half, and mounted on a cross sectioning holder for SEM imaging.

Sample Imaging

Samples were imaged using a Zeiss Ultra 55 field emission scanning electron microscope (FESEM) at an acceleration voltage of 7 keV, beam current of 190 pA, with a 30 µm aperture (on axis) and at 3.7 mm of working distance (WD). For imaging single digit features, we aim for the highest possible resolution. As a trade-off between resolution and beam damage, we chose 7 keV acceleration voltage; the HSQ was found to significantly damage at higher acceleration voltages. We also looked at the effect of reduced acceleration voltages, which is commonly known for dealing with charging[4,23]. For comparison between 1kV, 2.5kV and 7kV results using CPM coating see *Sup.* ***B***.
The detector used was the In-lens secondary electron, an annular detector located in the beam path above the objective lens that works combined with an electrostatic/ electromagnetic lens system. The electrostatic field acts as an acceleration field on the secondary electrons generated on the surface of the sample. The SE electrons are attracted, re-accelerated back towards the lens on a helical path and then focused through the electro-magnetic field to the SE In-lens detector. The signal from the In-lens detector is generated almost entirely through detection of secondary electrons generated by the primary electron beam (SE_1) and secondary electrons generated by backscattered electrons (SE_2)[35].
Image resolution was set to 1024 x 768 pixels with 8–bit gray-scale corresponding to a pixel size of 0.56 nm at 200k magnification and 0.27 nm at 400k magnification. Images were taken with pixel average and cycle time of 20.2 s corresponding to 25.6 µs dwell time per pixel. All images were carefully focused and astigmatism corrected on a different sample area than the recorded ones. The same stage tilt angle was used within an experiment. The SEM chamber was pumped down to 10^{-6} mbar prior to the measurements.

Contrast in the scope of this work

Generally contrast can be described as the difference in luminance or intensity between different locations[36]. This can refer to full images or localized areas within an image. Here we look at contrast between a specimen feature and its surrounding area (background). In an SEM, these local contrast differences can be affected by every variation of the signal along its processing path in the hard and software between the electron emission from the specimen and the display of the image.
For this work, contrast is not changed post-detection within the same experiment. Especially the contrast and brightness controls at the SEM were kept constant (for more details see *Sup.* ***C***). Therefore, contrast is looked at only pre-detection; meaning, that depending on the electron beam interaction with the specimen, contrast results as a consequence of the variation of SE yield and the trajectory of the electrons at different positions on the sample surface[37].

Method for quantification of contrast

In scanning electron microscopy and digital image processing and analysis, contrast is a broadly used term[38]. The quantification of contrast is therefore not intrinsically simple. It is usually either applied to quantitative or qualitative analysis or description, where the definition depends on the image, its content and/or the quantification purpose. Commonly used measures are Weber Contrast[39], Michelson

Contrast[39,40] and RMS contrast[39,40]. Those measures are not used in this work as their definitions do not fit our gray scale SEM image situation.

In order to quantify a change in contrast between a specimen feature and the background, we use image histogram information for image analysis. All histograms for this work are directly derived from non-normalized 8–bit SEM images. Histograms are used to determine the intensity range of the gray levels in an image. Essentially, in a grayscale image like that output from an SEM, each pixel has a gray level that represents intensity values[41]. The count of all pixels of that image at each gray value is depicted by its histogram. The spatial information for each pixel of the image is usually lost in the respective histogram. Therefore, we extract background and feature areas from the image and plot their sub histograms separately. Histograms are well suited, because data from a homogeneous area within the image does not have to be averaged and can be plotted with its full intensity distribution. Ideally, the background or feature have just one gray level value. However, this is usually not the case in SEM images. Instead, each sub-histogram is comprised of a range of intensities. As we target deep nanoscale features at high magnification (typically M>100k), feature and background will be comprised of areas of homogeneous appearance. Intensity values of such an area will be largely determined by noise[42]. This noise is statistical for the single pixel[42]. Therefore, the pixel intensities of the respective area will be largely uncorrelated and thus random with a distribution ideally symmetric to the average. By using a sufficiently large number of pixels of a homogeneous area, we can assume close to Gauss distributed intensities in the respective areas[43].

Figure ***2*** shows a schematic situation for two sub-histograms, which can be seen as background (S_b=blue) and feature (S_f=red) with ideal symmetric, Gauss distributed noise. In histograms, image contrast is usually seen from the overall range of intensity values (also called gray range or dynamic range), effectively used within a given image[44]. From the two distributions in *Figure* ***2****,* the intensity range is given by C_R.

In reality, the histograms will not be perfectly Gaussian. Therefore, the peak-to-peak distance of the S_b and S_f distribution, C_S, gives a more accurate measure of contrast between a feature and its background as it represents the gray level with most number of pixels for the visual perception. The more the two sub-histograms are separated from each other (larger C_S), the higher is the contrast between them. The width of the distribution is seen as noise[42]. Without perfect symmetry however, the full width at half max (FWHM), also gives a better measure of the noise, than the variance, which requires symmetry. In conclusion, a decrease in FWHM and an increase in the signal contrast increase the visual perception.

Note that visibility is actually a subjective term, which is individually different, but is in fact dependent on contrast and noise (*see Sup.* ***D*** *for an example*). An increase in contrast at the same noise level, can therefore just enable or improve visibility of features, which is especially important for smooth transitions at a specimen feature edge (*for an example see Sup.* ***E***), that are common in cross-sectional SEM at high magnification.

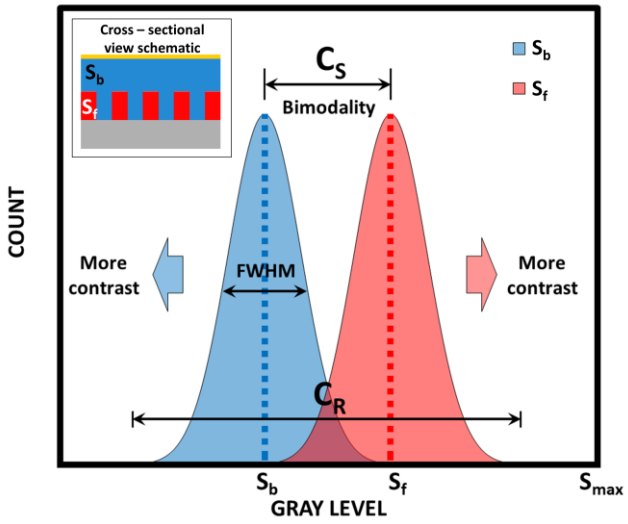

Figure 2: Schematic of an ideal histogram with two sub-histograms (blue and red) which can be seen as background and feature. Feature to background contrast increases with increasing C_S, the measure of the peak separation between the two distributions.

Electron-sample interaction in CS SEM

In CS SEM the accelerated electrons enter through the cross-sectional surface (CSS) and interact along the top surface (TS), *Figure* ***3***, close to a grazing incidence. Therefore, the bulk of the interaction volume is always close to both, TS and CSS, the sample surfaces. This increases the secondary electron yield.

Herein lies the challenge for high contrast imaging of small features at high magnification (M) by CS SEM. Every single pixel in the resulting image is now created by a superposition of secondary electrons emitted from two surfaces, TS and CSS. This is distinctly different from top down SEM, with one surface, where it is known that if the interaction volume is larger than the SE escape depth[4,45], tilting a sample increases the max secondary electron yield as well as the unity values of the electron yield as a function of electron energy[§], E_I and E_{II}, because the edge of the interaction volume intersects the sample edge.

The additional signal in CS SEM therefore has the potential to decrease the overall contrast in the image. This loss in contrast can be especially problematic when it comes to imaging features in the order or close to the SDR.

This work uses standard nomenclature for electron microscopy[4,46] and extends it to cross-sectional electron interactions shown in *Figure* ***3***:

PE are primary beam electrons.

SE_{1CSS} are hereby secondary electrons only generated by PE at the cross sectional surface.

SE_{1TS} are secondary electrons generated by PE but do escape from the top surface of the sample.

SE_{2CSS} are secondary electrons produced by backscattered electrons (BSE) and forward scattered electrons (FSE) that escape through the CSS.

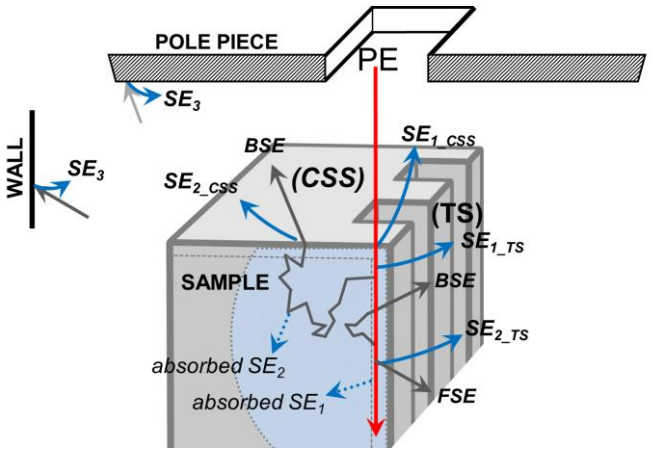

Figure 3: Schematic of cross sectional view showing interaction of primary beam (PE) with a sample within the SEM chamber. Electrons are emitted from top surface (TS) and cross sectional surface (CSS). The interaction volume is illustrated in gray.

SE_{2TS} are generated by backscattered and forward scattered electrons escaping from the top surface.

SE_3 are produced by scattered electrons at the walls of the SEM.

SE_4 are BSE and FSE detected as SE; note that SE_4 are named RE_4 in[46].

BSE Back scattered electrons.

FSE Forward scattered electrons.

Note that BSE, FSE, SE_3 and SE_4 are negligible for in-lens detection[4].

RESULTS & DISCUSSION

Figure ***4*** shows SE images of cross sections of sample type 1 comparing no coating, Au/Pd sputter coating, carbon coating, and conductive-polymer metal coating. The top row shows line patterns with 200 nm pitch (M=200k) and the bottom row shows 60 nm pitch patterns (M=400k). The center row histogram is derived from the area surrounded by the white dashed line in the top row picture. From this area, the actual shape of the feature was cut out and plotted in red, while the remaining area was plotted in blue. The patterned shape of the feature is what we are trying to image. Of the four images, the CPM coating produces the best image. The features can be seen easily against the background. In addition, the histogram shows the broadest intensity range and better defined bimodal distribution.

The uncoated sample produces the worst image. The overall feature-background contrast is very poor. The feature is actually not visible itself and just highlighted from its edges. Therefore, the histogram shows a darker feature and a brighter background. Furthermore, while the 200 nm pitch features are visible, it is difficult to discern interfaces between materials. In the M=400k image, a 'ghost' line appears between chromium and HSQ, obscuring the actual shape of the chromium undercut. This indicates an electric field buildup on the surfaces which can deflect the incident beam and escaping secondaries. In general, the secondary electron yield, δ, is a strong function of the primary beam energy[47,48]. The buildup of a retarding electric field will therefore increase δ by some degree[49] but will still degrade image formation.

In *Figure* ***4****, 2nd column*, features are sputter coated with a ***Au/Pd*** alloy which is preferred over pure gold as the alloy discourages epitaxial growth, leading to a reduced surface roughness[3,34]. The high conductivity of this alloy prevents static charge accumulation. The top surface of the sample lights up as the beam scans in a shallow angle, because more secondaries along the beam path have the chance to escape. Differences between features and coating are difficult to see. We can understand why by looking at the secondary electron yield δ of the materials. Yield can be estimated as a function of primary beam energy E_{PE} (in keV) and maximum yield δ_m. By using the semi-empirical approach[47], $\delta = 0.86 \times \delta_m^{1.35} \times (E_{PE}[keV])^{-0.35}$, the electron yield at 7 keV is 0.44 for Cr,

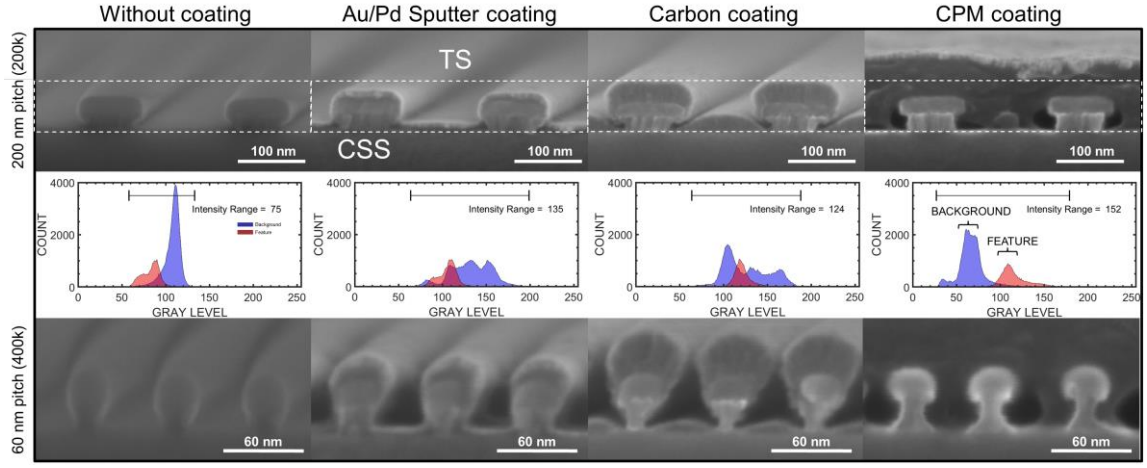

Figure 4: SE images and histograms of intensity of gray levels cross sectioned from sample type 1 with different coatings. From left to right: **1)** without coating, **2)** Au-Pd sputter coating, **3)** carbon coating, and **4)** conductive polymer-metal coating. **Top row:** 200 nm pitch, imaged at 200k magnification; **Center row:** histogram of area marked by dashed line, where feature contour was cut out (red), while remaining background is shown in blue. Note that CPM shows bimodal distribution between features and background. **Bottom row:** 60 nm pitch, imaged at 400k magnification.

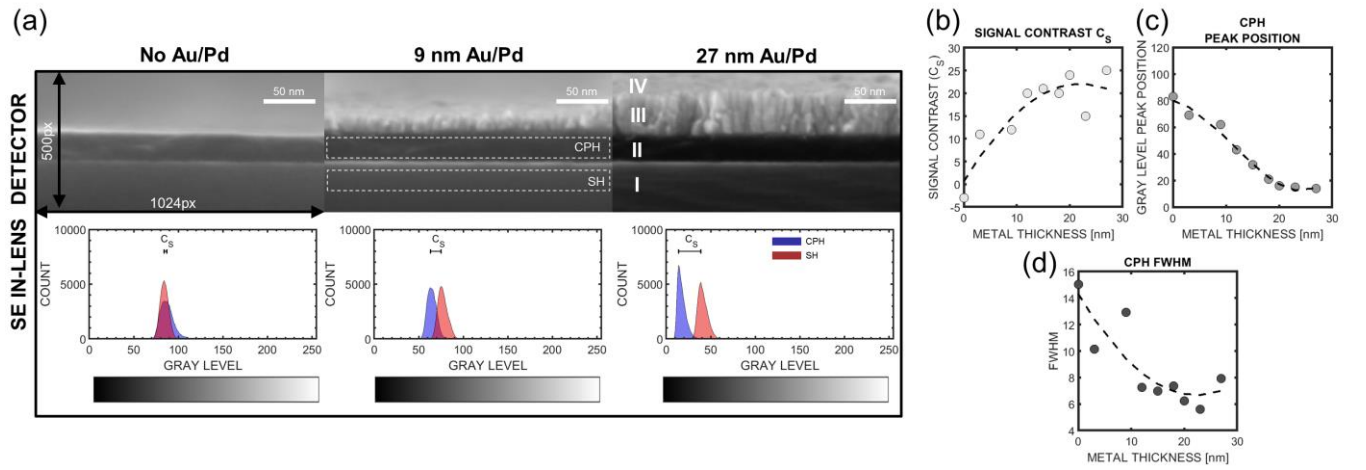

Figure 5: (a) SE image of a simplified cross-section for quantification of contrast using a stack of silicon (I), conductive polymer (Aquasave) (II), Au/Pd sputter layer (III) and top of the sample (IV) in a 1024x500 pixel size image at 200k magnification and 7 keV EHT. The corresponding histogram of intensity gray leves from areas (I) and (II) were generated from the white dash outlined areas of 60 x 1024 pixels. The conductive polymer histogram (CPH) is shown in blue and the silicon histogram (SH) in red SE images and corresponding histogram of 3 out of 9 images. **(b)** C_S as a function of metal thickness, **(c)** CPH peak position as function of metal thickness and **(d)** FWHM of CPH as function of metal thickness.

0.68 for Au, and 0.60 for Pd. These yields are relatively similar, so the Au/Pd coating hampers discriminability and thus obscures the shape of the undercut Cr, particularly in the 60 nm pitch lines. In addition, at 60 nm pitch, discontinuity in the coating allows the HSQ to charge, which limits the ability to see the Cr/HSQ interface. This brightness can also arise because the CSS is not coated. The overall contrast is higher than in the non-coated sample case, but an overlap in feature-background histograms and the lack of bimodality prevent the measurement of signal-contrast. Note, that it was found that HSQ immediately shrinks upon e-beam irradiation which can be seen in the darker area between HSQ and Au/Pd coating.

Evaporated carbon coating is shown in *Figure **4**, 3rd column*. The top image shows that HSQ and chromium can be distinguished, and boundaries are visible. It is interesting to note that despite a similar coating discontinuity in both the 60 nm and 200 nm pitch features, no charging appears and good carbon/feature contrast can be seen. The higher contrast between Cr and C is due to the ratio between SE_1 (δ_1) and SE_2 (δ_2) yield. The total SE yield[46] is $\delta_T = \delta_{SE1} + \delta_{SE2}$, where $\delta_{SE2} = f(\eta)$, and thus also depends on the BSE coefficient η. Au-Pd is a high atomic-number material and has a much stronger η than carbon. However, the total yield of carbon is about ¼ that of pure gold[3], making it a good background coating material. Unfortunately, a crisp feature view is obscured by the change of coating thicknesses on the top of the feature and the trench. The intensity range shown in the histogram is similar to that of Au/Pd, but there is also no distinct bimodal distribution, due to histogram overlap and a broad background distribution. Comparing no coating, metal coating, and carbon coating, the carbon coating is the best. However, carbon coating does have downsides. Carbon evaporation can create particle contamination and is thus undesired in cleanrooms. Carbon rod sources produce graphite dust and residue during handling. An alternative to rods, carbon fibers, tend to fall down onto the sample. Also, the thickness during carbon evaporation is more difficult to control than during sputtering.

Polymer metal coating, using conductive polymer, is pictured in the right column of *Figure **4***. It can be seen directly from the images that features of interest are clearly visible and have high contrast against the conductive polymer. The image contrast is not only enhanced by large intensity range, but also by the clear intensity separation of those areas. The histogram clearly reveals bimodality between background and feature. As a consequence, the undercut chromium and HSQ layer are easily distinguishable from the conductive polymer. The coating also surrounds the features almost completely. Voids between substrate and features do occur, but show no evidence of charging as the film is fairly continuous. Also, note that the metal alloy sputtered on top allows easy focusing and stigmation correction using the grain structure of the Au/Pd film. The CPM coating clearly shows the best imaging properties of the films tested. In the following section we address the importance of the metal coating in CPM and how to optimize its value.

Effect of metal layer thickness

To investigate the effect of the metal layer thickness on contrast in CPM coating, we used a stack without patterned features and varied the sputter layer thickness in 9 samples from no metal coating to 30 nm thick. The sample layout is shown in *Figure* **5***a right* with the stack consisting of silicon (I), conductive polymer (II), Au/Pd sputter coat (III). The top of the Au/Pd coat is visible due to a 0.7 deg stage tilt and is noted as (IV). The conductive polymer coating thickness of 28 nm (±2 nm) was the same in all cases. The histogram of the conductive polymer (CPH) was plotted in blue and the silicon histogram (SH) in red. Both were derived from an area of 1024 x 60 pixels (surrounded by white dashed line in *Figure* **5***a center*).

*Figure **5a*** shows SE images from the in-lens detector (ILD). Three images are shown for the case of no Au/Pd coating,

9 nm and 27 nm Au/Pd coating, as well as their corresponding CPH and SH. From these histograms we measured the signal contrast C_S (*Figure* **5***b*), conductive polymer (background) peak position (*Figure* ***5****c*), and conductive polymer (background) FWHM (*Figure* **5***d)*, all plotted against metal thickness.

Plots show that with increasing metal layer thickness (*Figure* **5***b)* the signal contrast C_S increases. Importantly, the conductive polymer becomes darker, as seen by a decrease of the CPH peak position (*Figure* **5***c*). This shows that an increase in metal layer thickness has an effect on the secondary electron yield from the polymer and silicon area. Both distributions shift left, meaning less signal reaches the detector, but the overall signal contrast C_S increases, as the shift is stronger on the polymer area. Also, with increasing metal layer thickness there is a trend of decreasing CPH FWHM (*Figure* **5***d*). With increasing metal layer thickness the signal emerging from the CPH area is more homogenous. This means that the gray level distribution of SE detected per pixel becomes narrower, meaning a decrease in the signal to noise ratio, S/N.

Discussion on secondary electron yield

SEs detected by the in-lens detector are usually thought to be almost exclusively[35] SE_1 and SE_2. Therefore, the observed effects with changing metal thickness must all be attributed to changes in the secondary electron yield within the silicon and the conductive polymer layer. However, in CS SEM, SE can emit from the cross-sectional surface as SE_{1CSS} and SE_{2CSS}, and from the top surface as SE_{1TS} and SE_{2TS}. This can be seen, for example, in region III and IV of *Figure* ***5****a*, showing the top surface and cross-sectional surface of the Au/Pd layer with same brightness. Due to the low energy of those secondaries from the top surface, they can be easily deflected by the in-lens electric field and thus act as an additional secondary electron source. The effect of the metal layer on the contrast between silicon and polymer, must therefore originate from the total SE yield

$$\delta_T = \delta_{SE1CSS} + \delta_{SE1TS} + \delta_{SE2CSS} + \delta_{SE2TS} \qquad \text{(eq. 1)}$$

in each region of *Figure* ***5***.

Before we look at the yields for SE_1 and SE_2 in separate, we must have a look at the effect of high density materials, such as metal, on secondary electrons in general. For high density materials, such as metals, the mean escape depth λ is on the order of 0.5 nm to 1.5 nm ([46,49,50]). In the case of Au[50] λ is 0.5 nm and for Pd[50] λ is 1 nm. Therefore, even thin continuous metal films can block secondary electrons by absorption.

Relating now to the total SE yield, we first look at the SE_1 related yield (SE_{1CSS} and SE_{1TS}), which is generated by the primary beam and ask, what is the effect of the metal layer on SE_1 in the two different regions of *Figure* **5***,* silicon and polymer. Seiler[46] estimated the escape diameter of SE_{1CSS} to $d = \sqrt{d_0^2 + \lambda^2}$, where d_0 is the primary beam diameter. For d_0=1 nm and[50] $\lambda_{Si} = 2.7\ nm$, d would be 2.9 nm. Therefore the SE_{1CSS} signal generated in the silicon would not be affected by a metal layer 50 nm away. For Aquasave, the conductive polymer, the escape depth is unknown, but it is known that polymers have larger mean escape depth[51,52], in the order of up to 20 nm. Assuming, that the SE_{1TS} signal decreases with distance x into the surface[46] by $e^{-x/\lambda}$, the maximum escape depth[46,53] T is about 5λ. Therefore the majority of SE_{1TS} would emit from an area with diameter of $d = 20\ nm$, while some SEs also could emit up to $d = 100\ nm$. Therefore, the SE_{1CSS} signal generated in the polymer will be increasingly affected, the closer the beam moves towards the metal layer. However, even for $\lambda = 20\ nm$, the majority of SE_{1CSS} will not be affected up to 10 nm proximity to the metal layer. For SE_{1TS}, the effect will be even smaller, due to the proximity requirement. Therefore, the ratio of δ_{SE1CSS} to δ_{SE1TS} will be strongly on the SE_{1CSS} side, concluding that SE_{1TS} are an almost insignificant contribution to the total signal, while both signals, SE_{1CSS} and SE_{1TS}, will be unaffected on the Silicon by addition of a metal layer.

For SE_{2CSS} and SE_{2TS}, the situation is different. The yields of SE_{2CSS} and SE_{2TS} are dependent on the material density and are proportional[47] to the scattered electron yield η. The yield η is usually attributed to just BSE, but in a CS SEM setup, electrons can also scatter and leave at angles of >90 deg. Therefore, we here also count FSE to this yield.

When the primary electron beam hits the CSS, high energetic BSE and FSE are created, which can travel much longer distances than secondary electrons. While leaving the sample from the TS or the CSS, BSE and FSE can generate secondary electrons, which emit isotropically in a cosine distribution relative to the sample surface[3,47]. The escape radius for secondary electrons, generated by BSE, r_{SE2}, can be estimated[4,54] from bulk material interaction to be $r_{SE2} = R_B/3$. R_B is the Bethe range of electrons, approximated by $R_B = 76\ E^{1.66}/\delta_m$ (nm) with mass density δ_m (g/cm³) and beam energy E in keV. Accordingly, the escape radius of BSE and subsequently SE_2, at 7 keV is 39 nm for Au/Pd (ratio 60/40) and 278 nm for silicon. For Aquasave, the conductive polymer, the mass density is unknown but can be estimated[55] to be 1.4 g/cm³ and thus gives $r_{SE2} \approx 458$ nm. Therefore, BSE, generated in the silicon and polymer can cross the metal layer, which then create SE_{2CSS} and SE_{2TS} on the metal surface. Thick metal layers however can affect BSE and FSE by scattering and absorption. In consequence, the reduced SE_2 yield would decrease the total signal. This however does not fully explain the stronger intensity decrease of the polymer layer with increasing metal layer thickness and therefore requires further analysis.

Monte Carlo simulation of BSE and FSE

Here, we employ the use of Monte Carlo simulations using CASINO[56,57] to account for the total yield of BSE and FSE. CASINO is a powerful free 3D electron simulation software which allows for modelling backscattered and transmitted electron signals[56]. For this work we use BSE and FSE modelling as a proxy for the SE_2 yield, which will be proportional and is mainly dependent on the material density (for details see *Sup* ***F***) .For the simulation, we created a 3D version of the stack of *Figure* **5***,* with Silicon, 50 nm Polyaniline, and Au/Pd (60/40)

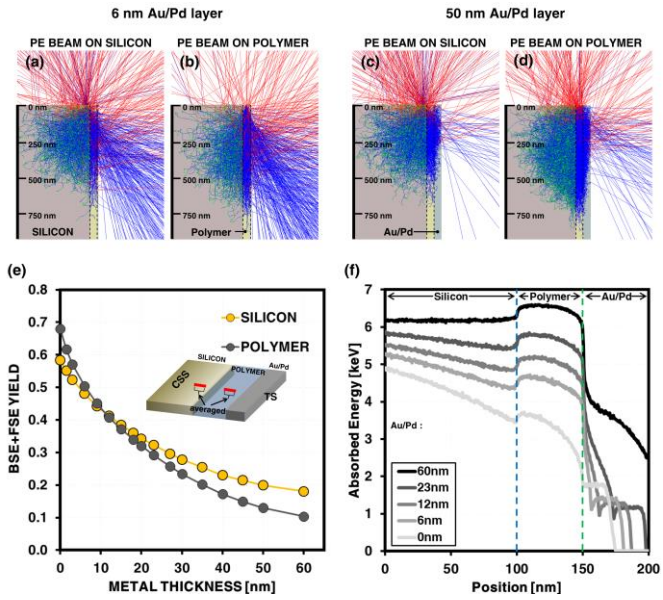

Figure 6: Monte Carlo simulation of BSE and FSE yield. **(a-d)** Sideview of cross-section for case of 6 nm Au/Pd on silicon part (a) and Polymer part (b) and 50 nm Au/Pd on silicon part (c) and polymer part (d). BSE (red) and absorbed/FSE (blue) trajectories are shown. Note that the interaction volume stretches deeper, when the beam is on the polymer layer. **(e)** Simulation of BSE+FSE yield at 0.7 deg tilt (like *Figure 5*) as function of the metal layer thickness. 26 data points with 10000 electrons each were simulated across 10 nm and averaged for the polymer layer and the silicon layer. Note that the yield from the polymer layer decreases stronger than the yield from the silicon layer. **(f)** Absorbed Energy as function of Position, across a 200 nm line scan from the silicon layer to the Au/Pd layer for different Au/Pd thicknesses. Note that absorption is strongest in the polymer layer.

with varying thickness. In *Figure* **6**, a side view of the cross section simulation results for 6 nm Au/Pd (*Figure* **6**a,b) and 50 nm Au/Pd (*Figure* **6**c,d) is shown. The primary beam at 7 keV hits the sample either in the center of the polymer layer (*Figure* **6**b,d), or into the silicon layer at 25 nm from the Si/Polymer interface (*Figure* **6**a,c). 1000 electrons were simulated for display. BSE (red) and FSE (blue) and absorbed electrons (blue) are shown with their trajectories. Electrons leaving the sample, show straight lines emerging from the surface. Clearly, the position of the primary electron beam, changes the number of scattered electrons and their ratio from CSS to TS direction. For the 6 nm layer, the BSE yield decreases, when the beam hits the polymer (*Figure* **6**b), compared to the silicon layer (*Figure* **6**a). Increasing the metal thickness to 50 nm, increases the BSE yield in (*Figure* **6**d), compared to (*Figure* **6**b), while the overall yield is decreased. Also, the interaction volume stretches deeper into the sample when the beam hits the polymer (*Figure* **6**b,d), compared to the silicon layer (*Figure* **6**a,c), due to the difference in mass density.

We looked at the total yield (BSE and FSE) of all electrons leaving the sample, depending on whether the primary beam is on the silicon or the polymer layer. By scanning along a 10 nm distance perpendicular to TS, with 0.4 nm spacing, we simulated 10000 electrons per data point and calculated the arithmetic mean, shown as BSE+FSE yield in *Figure* **6***e.* First we can observe, that both curves decrease with increasing metal layer thickness. This means, that the total yield of BSE and FSE, and therefore also the yield of SE_2, decrease. This can be explained, with the metal layer increasingly hindering BSE and FSE from leaving the sample through the TS. These electrons therefore are absorbed and do not contribute to SE_{2TS} generation. This is consistent with the trend observed in *Figure* 5*d,* where the gray level of the conductive polymer histogram decreases with the increase of the metal layer thickness.

Additionally, the BSE and FSE yield in case of the primary beam on the polymer layer decreases faster than in case of the primary beam on the silicon layer. This behaviour is due to the stronger absorption of the polymer layer. *Figure* **6***f* shows line scans from the silicon layer to the Au/Pd layer for different thicknesses. Possibly, the lower density of the polymer with two higher density materials on its flanks, acts similar to a faraday cup by preventing electrons to escape and being absorbed. The differential decrease of the BSE+FSE yield on TS and CSS, changes the SE_2 emission accordingly, which results in

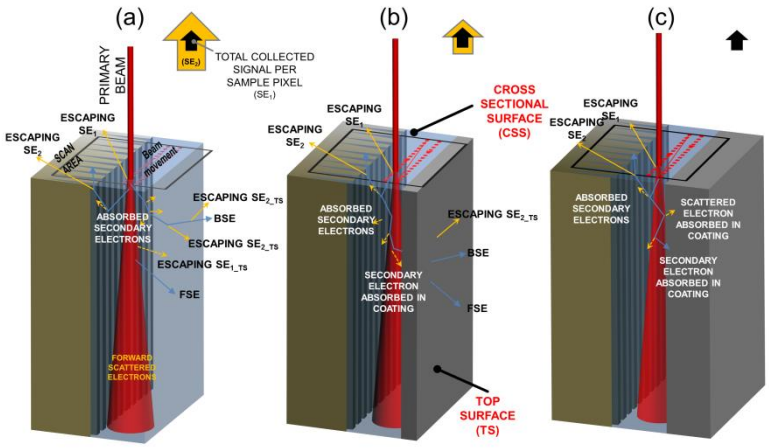

Figure 7: Schematic view of cross-section under electron beam exposure showing cross-sectional surface (CSS) and top surface (TS) of the sample. Interaction of the electron beam with the sample creates multiple secondary and scattered electrons to be considered for detector signal generation. Arrows schematically indicate changes in detected SEs from SE_1 (black) and SE_2 (yellow). ***(a):*** without blocking layer; all escaping SE from the polymer contribute to image pixel signal. **(b)***:* thin metal layer; ***(c):*** thick metal layer.

a faster decrease of the CPH compared to the SH in *Figure* **5***c*. This decrease, therefore is consistent with the increase in signal contrast C_S.

The decrease of the SE_2 yield (SE_{2CSS} and SE_{2TS}) with increasing metal layer thickness, changes the $\delta_{SE1}/\delta_{SE2}$ ratio towards SE_1 detection. SE_2 acts as a noise component to the high resolution SE_1 signal. Thus reducing the SE_2 contribution, improves the signal to noise ratio (compare *Figure* **5***e).*

In conclusion, the effect of the metal layer on contrast between the silicon and the polymer showing increasing C_S, can be attributed to the stronger reduction of SE_2 in the polymer due to enhanced absorption.

Figure ***7*** illustrates comprehensively the proposed mechanism in the case of different scenarios of no Au/Pd layer, thin Au/Pd layer and thick Au/Pd layer. The attenuation of the SE_2 signal component increases the high resolution SE_1 component. The arrows illustrate the reduction of SE_2 yield (yellow) with remaining SE_1 yield (black).

Application in high-resolution imaging

To address the benefit of polymer-metal coating for high resolution imaging on SiO_2 features, we compared the effect of metal layer thickness on tapered features of sample type 2, SiO_2 patterned features. *Figure* ***8*** shows the effect on samples of 30 nm pitch features having no Au/Pd (conductive polymer only), 6 nm (thin) and 50 nm (thick) Au/Pd sputter coating. Top row images are all taken at same conditions without any image post processing, but additional image dwell time of 30 s was required to make features visible in the no coating case. Adding a thin metal layer immediates image acquisition (short dwell time). Second row shows magnified SEM images from top row to bring out 15 nm trenches with sub–5 nm at the bottom in better detail.

Without any metal coating*, Figure* ***8*** left column shows poorer contrast between the conductive polymer and the SiO_2 features which becomes especially apparent near the trench bottom where visibility is reduced. In some cases features were clearly visible when edges went bright, likely due to negative charge build up as the polymer shrinks, exposing the feature surface. Although increasing magnification does not alter the beam current, it does lead to a higher electron dose due to the smaller scan area[46]. A further downside of imaging without a coating at long dwell times is the possible swelling of features due to prolonged electron beam exposure. Furthermore, with no metal coating, the conductive polymer was damaged more. This may be because when the metal layer is present, it acts as heat sink and efficient electrical conductor, minimizing damage.

On the other hand, addition of sputtered Au/Pd on the conductive polymer increases contrast with a 50 nm Au/Pd coating, leading to a high contrast polymer layer against the silicon. In addition, surface details of the polymer layer are only visible with metal coating.

Figure **8** shows that visibility overall is improved by adding a metal layer. On the one hand, PMC has an effect on the visibility by improving the S/N ratio (see Sup. D). On the other hand, contrast enhancement by adding a metal layer,

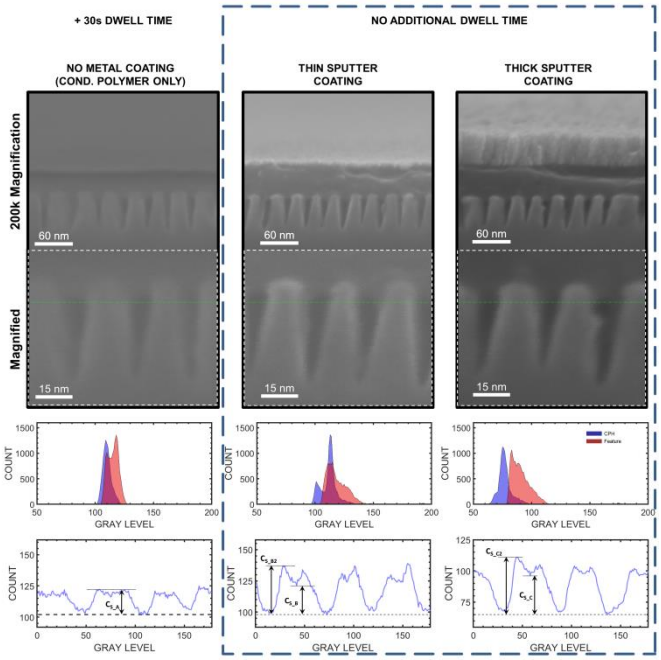

Figure 8: SE images and histograms of gray levels comparing CPM coating using different metal thickness. Left, no Au/Pd sputter coating (long dwell time), middle 6 nm Au/Pd and right 50nm Au/Pd (both direct imaging, same dwell time). Sample type 2: bare etched SiO_2, 30 nm pitch. ***2nd row:*** Magnified images from top row to show trenches in greater detail. **3rd row:** Corresponding histograms of gray levels of 2nd row images. **4th row:** Signal intensity along green line in magnified images. Note that edge effects can enhance visibility, by increasing the edge to background contrast. Center feature to background contrast increases with metal thickness. Also note that sub-5 nm trench bottom is much better visible with metal coating.

improves the visibility as well. Visibility can, however, also be enhanced by edge contrast caused by enhanced emission from the larger surface at the edge. *Figure* **8** *4th row* shows the intensity profile along the green line in the magnified image of *Figure* **8** *2nd row.* Edge emission enhances contrast at the edge and therefore visibility.

Furthermore, we do not see charging as a main contributor to visibility enhancement, as charging in general would cause beam dispersion or deflection and thus a decrease in resolution. *Figure* **8** *middle and right* images clearly show the 5 nm trench bottom after metal layer addition. Also, it can be expected, that the metal layer increases the overall conductivity of the sample top surface and therefore discourages charge accumulation. On the other hand, the resolution loss in *Figure* **8** *left* without Au/Pd coating could have its origin in a charge accumulation.

Note that with addition of Au/Pd coating we did not observe much polymer damage over time. The uncoated conductive polymer has more surface exposed to atmosphere. This can allow water absorption and swelling which over time obstructs the features. Adjusting post image processing contrast and brightness individually could further enhance the image and can offer high image contrast with the conductive polymer. Also, for single-digit features with fairly large aspect ratio, PMC in general can act as mechanical support, preventing damages while cleaving the sample.

Alternate use of PMMA or carbon for the polymer layer

Because the mechanism described is not limited to the use of conductive polymer, we also investigated PMMA as a readily available and cheap alternative. For details on the results see *Sup.* ***G***. We conclude from this, that PMMA also works, but polymers with better beam stability, like the conductive polymer used in this work, would be preferred.

To address the question of whether the use of carbon would be beneficial for stacked coating either as a substitute for the polymer or the metal layer, we also tested Au/Pd on evaporated carbon instead of polymer (*Sup.* ***H***). Carbon is of low density, and therefore also fulfils the mechanism requirement. However, it was found that evaporated carbon does not cleave as nicely as the PMC samples. Overhangs are common leading to obscured features and causing issues during imaging. Poorly cleaved carbon meant good spots for imaging were the exception rather than the rule. In addition, as mentioned earlier, carbon is problematic in clean rooms.

Sample Cleaning of polymer-metal coated samples

An advantage of using polymer metal coating instead of carbon or Au/Pd coating is the possibility to remove the coating by lift-off in a suitable solvent. Conductive polymer metal coating using Aquasave as conductive polymer can be removed after imaging by simply immersing the coated sample in water as solvent. Results after CPM water removal from a fingerprint block copolymer sample are shown in *Sup.* ***I***. Aquasave dissolves quickly in water and lift-off of 20 nm layers occurred immediately by solvent attack from crack in the Au/Pd layer. In case of thicker layers, lift-off is dependent on the sample size. Other polymers require appropriate solvents to lift-off the Au-Pd layer. This removability of the coating also allows for creation of monitoring samples which can be used at different steps in a process. For example, a larger sample can be used multiple times; after each step the PMC can be removed, making the remainder of the monitoring sample reusable.

In comparison, the removal of coated carbon or sputtered metals is more difficult. Carbon can be removed by oxygen plasma and metals require wet chemical or plasma treatment which both can damage the under lying material.

Further comments - other benefits of Polymer-Metal Coating

Sample contamination has not been seen to be an issue. Even if polymer-metal coated samples are imaged weeks after cleaving, image results do not show charging or darkening. The SEM used is very clean, and pressure was maintained below 5E-5 bar during imaging. Damaging of PMC samples during imaging has not been seen to be an issue. The exposed damaged area is within a frame in the order of usually 0.1 µm², which is not a source of sufficient material for contamination. Note that PMC is compliant with cleanroom fabrication, but does not require a cleanroom.

One can speculate that PMC is also usable for nanoparticle imaging by suspending those into the resist. Also, imaging biological samples might be possible with CMP, as the conductive polymer is dissolved in water.

Conclusions

A new chip-based sample preparation method for cross-sectional SE imaging has been presented. A stacked layer of spin coated polymer and sputtered metal exhibited great ability to discern etching feature profiles and materials interfaces of densely packed nano-patterned features. CPM coating was found to give better SE image contrast than either polymer, Au/Pd sputter, or carbon coating alone. Signal contrast, C_S, increased while FWHM of the feature and background gray level distribution decreased with the increasing of the metal layer thickness. Monte Carlo simulation of backscattered and forward scattered electrons suggests that as the metal layer thickness increases, the amount of SE_2 leaving the samples through TS is reduced. More importantly, the reduction in SE_{2TS} is more pronounced in the polymer layer than in the silicon layer due to enhanced absorption in polymer and that is possibly the main reason for the increase in SE signal contrast. High magnification SE images of 30 nm pitch trenches coated with CPM exhibited clear view of sub-5 nm trench bottom. The conductive polymer Aquasave was found to be highly stable against beam damage. Conductive polymer metal coating using Aquasave can be removed after imaging by simply immersing the coated sample in water. We conclude that CPM coating is a new, fast and cleanroom compliant method for generating cross-sections SE images capable of single-digit feature imaging with high contrast.

Conflicts of interest

There are no conflicts to declare.

Acknowledgements

We thank Scott Dhuey, Simone Sassolini, Michael Elowson and Arian Gashi for their technical assistance in the cleanroom at the Molecular Foundry. We also thank Zhaoning Yu from Seagate Technology LLC for his support. Furthermore, we are especially grateful to Seagate Technology LLC for support of D. S. We thank S. Cabrini for critical reading of the manuscript. This work was completed at the Molecular Foundry and supported by the Office of Science, Office of Basic Energy Sciences, of the U.S. Department of Energy under Contract No. DE-AC02-05CH11231. DO and VA were supported by this contract. A part of this research has received funding from the European Union's Seventh Framework Programme FP7/2007-2013 under Grant No. 318804 ("Single Nanometer Manufacturing for beyond CMOS devices" — acronym SNM).

Notes and references

§ E_I and E_{II} refer to the well known electron yield vs. electron energy curves, where the electron yield increases with energy to a max. value E_p (typically between 300

eV and 1 keV) and then decreases. The E_I and E_{II}[§] values denote where electron emission and absorption are equal[46]

1 P. W. Hawkes and J. C. H. Spence, *Science of Microscopy*, Springer Science+Business Media, LLC, New York, Volume I., 2007.
2 K. C. A. Smith and M. A. Oatley, *Br. J. Appl. Phys.*, 1955, **6**, 391–399.
3 J. Goldstein, D. Newbury, D. Joy, C. Lyman, P. Echlin, E. Lifshin, L. Sawyer and J. Michael, *Scanning Electron Microscopy and X-Ray Microanalysis*, Springer Science+Business Media, New York, 3rd edn., 2007.
4 D. C. Joy and C. S. Joy, *Micron*, 1996, **27**, 247–263.
5 D. C. Joy, *Ultramicroscopy*, 1991, **37**, 216–233.
6 X. Yang, Y. Xu, K. Lee, S. Xiao, D. Kuo and D. Weller, *IEEE Trans. Magn.*, 2009, **45**, 833–838.
7 I. Ferain, C. A. Colinge and J.-P. Colinge, *Nature*, 2011, **479**, 310–316.
8 T. Ito and S. Okazaki, *Nature*, 2000, **406**, 1027–1031.
9 ITRS, *International Roadmap of Semiconductors 2.0 (ITRS) - Lithography Tables*, 2015.
10 ASTC, ASTC Technology Roadmap, http://www.idema.org/?page_id=5868.
11 I. W. Rangelow, A. Ahmad, T. Ivanov, M. Kaestner, Y. Krivoshapkina, T. Angelov, S. Lenk, C. Lenk, V. Ishchuk, M. Hofmann, D. Nechepurenko, I. Atanasov, B. Volland, E. Guliyev, Z. Durrani, M. Jones, C. Wang, D. Liu, A. Reum, M. Holz, N. Nikolov, W. Majstrzyk, T. Gotszalk, D. Staaks, S. Dallorto and D. L. Olynick, *J. Vac. Sci. Technol. B*, 2016, **34**, 1–13.
12 R. Garcia, A. W. Knoll and E. Riedo, *Nat. Nanotechnol.*, 2014, **9**, 577–587.
13 C. Peroz, S. Dhuey, M. Cornet, M. Vogler, D. Olynick and S. Cabrini, *Nanotechnology*, 2012, **23**, 1–5.
14 B. Päivänranta, A. Langner, E. Kirk, C. David and Y. Ekinci, *Nanotechnology*, 2011, **22**, 375302.
15 M. Park, C. Harrison, P. M. Chaikin, R. A. Register and D. H. Adamson, *Science (80-.).*, 1997, **276**, 1401–1404.
16 H. S. Suh, D. H. Kim, P. Moni, S. Xiong, L. E. Ocola, N. J. Zaluzec, K. K. Gleason and P. F. Nealey, *Nat. Nanotechnol.*, 2017, **12**, 1–9.
17 D. Zhao, J. Feng, Q. Huo, N. Melosh, G. H. Fredrickson, B. F. Chmelka and G. D. Stucky, *Science (80-.).*, 1998, **279**, 548–552.
18 S. O. Kim, H. H. Solak, M. P. Stoykovich, N. J. Ferrier, J. J. de Pablo and P. F. Nealey, *Nature*, 2003, **424**, 411–414.
19 H. S. Moon, J. Y. Kim, H. M. Jin, W. J. Lee, H. J. Choi, J. H. Mun, Y. J. Choi, S. K. Cha, S. H. Kwon and S. O. Kim, *Adv. Funct. Mater.*, 2014, **24**, 4343–4348.
20 B. Bunday, E. Solecky, A. Vaid, A. F. Bello and X. Dai, in *Proc. of SPIE*, 2017, p. 101450G.
21 T. R. Albrecht, H. Arora, V. Ayanoor-Vitikkate, J. M. Beaujour, D. Bedau, D. Berman, A. L. Bogdanov, Y. A. Chapuis, J. Cushen, E. E. Dobisz, G. Doerk, H. Gao, M. Grobis, B. Gurney, W. Hanson, O. Hellwig, T. Hirano, P. O. Jubert, D. Kercher, J. Lille, Z. W. Liu, C. M. Mate, Y. Obukhov, K. C. Patel, K. Rubin, R. Ruiz, M. Schabes, L. Wan, D. Weller, T. W. Wu and E. Yang, *Ieee Trans. Magn.*, , DOI:Artn 080034210.1109/Tmag.2015.2397880.
22 I. W. Rangelow, *J. Vac. Sci. Technol. A Vacuum, Surfaces, Film.*, 2003, **21**, 1550–1562.
23 M. M. Mirza, H. Zhou, P. Velha, X. Li, K. E. Docherty, A. Samarelli, G. Ternent and D. J. Paul, *J. Vac. Sci. Technol. B, Nanotechnol. Microelectron. Mater. Process. Meas. Phenom.*, 2012, **30**, 06FF02.
24 D. Ze-Jun and R. Shimizu, *J. Microsc.*, 1989, **154**, 193–207.
25 M. Tanaka, C. Shishido, Y. Takagi, H. Morokuma, O. Komuro and H. Mori, in *Proc. of SPIE*, 2003, pp. 624–635.
26 M. T. Postek, 1994, **10274**, 1027405.
27 D. B. Williams and C. B. Carter, *Transmission Electron Microscopy*, Springer Science+Business Media, LLC, 1996, vol. 13.
28 D. C. Joy, *AIP Conf. Proc.*, 2003, **683**, 619–626.
29 D. C. Joy, Y.-U. Ko and J. Uwu, in *Proc. of SPIE*, 2000, vol. 3998, pp. 108–114.
30 D. Staaks, X. Yang, K. Y. Lee, S. D. Dhuey, S. Sassolini, I. W. Rangelow and D. L. Olynick, *Nanotechnology*, , DOI:10.1088/0957-4484/27/41/415302.
31 J. Teshima and J. J. Clarke, *Solid State Technol.*, 2014, 21–26.
32 W. Hu, T. Orlova and G. H. Bernstein, *J. Vac. Sci. Technol. B*, 2002, **20**, 3085–3088.
33 J. Kim, Y. W. Jeong, H. Y. Cho and H. J. Chang, 2017, **47**, 77–83.
34 P. Echlin, *Handbook of Sample Preparation for Scanning Electron Microscopy and X-Ray Microanalysis*, Springer Science+Business Media, LLC, New York, 2009.
35 Zeiss - Manual for the Supra (VP) ULTRA scanning electron microscopes, 2005.
36 S. Inoué, *Video Microscopy*, Springer Science+Business Media, 1986.
37 J. I. Goldstein, D. E. Newbury, J. W. Colby, H. Yakowitz, E. Lifshin and J. R. Coleman, *Practical Scanning Electron Microscopy - Electron and Ion Microprobe Analysis*, Plenum Press, New York and London.
38 E. Peli, *J. Opt. Soc. Am. A.*, 1990, **7**, 2032–2040.
39 D. G. Pelli and P. Bex, *Vision Res.*, 2013, **90**, 10–14.
40 P. J. Bex and W. Makous, *America (NY).*, 2002, **19**, 1096–1106.
41 E. Reinhard, M. Stark, P. Shirley and J. Ferwerda, *ACM Trans. Graph.*, 2002, **21**, 267–276.
42 D. C. Joy, *Biol. low-voltage scanning electron Microsc.*, 2008, 129–144.
43 P. Réfrégier, *Noise Theory and Application to Physics - From Fluctuations to Information*, Springer Science+Business Media, New York, 2003.
44 W. Burger and M. J. Burge, *Digital image processing - An Algorithmic Introduction Using Java*, Springer-Verlag, London, 2nd editio., 2016.
45 T. Ichinokawa, M. Iiyama, A. Onoguchi and T. Kobayashi, *Jpn. J. Appl. Phys.*, 1974, **13**, 1272–1277.
46 H. Seiler, *J. Appl. Phys.*, , DOI:10.1063/1.332840.
47 K. Kanaya and H. Kawakatsu, *J. Phys. D. Appl. Phys.*, 1972, **5**, 1727–1742.
48 K. Kanaya, S. Ono and F. Ishigaki, *J. Phys. D. Appl. Phys.*, 1978, **11**, 2425–2437.
49 C. Bouchard and J. D. Carette, *Surf. Sci.*, 1980, **100**, 251–268.
50 Y. Lin and D. C. Joy, *Surf. Interface Anal.*, 2005, **37**, 895–900.
51 R. F. Willis and D. K. Skinner, *Solid State Commun.*, 1973, **13**, 685–688.
52 D. L. Vezie, E. L. Thomas and Anonymous, *Polymer (Guildf).*, 1995, **36**, 1761–1779.
53 R. Hessel and B. Gross, *IEEE Trans. Electr. Insul.*, 1992, **27**, 831–834.
54 C. Feldman, *Phys. Rev.*, 1960, **117**, 455–459.
55 J. Stejskal, I. Sapurina, M. Trchova, J. Prokes, I. Krivka and E. Tobolkova, *Macromolecules*, 1998, **31**, 2218–2222.
56 H. Demers, N. Poirier-Demers, A. Réal Couture, D. Joly, M. Guilmain, N. de Jonge and D. Drouin, *Scanning*, 2012, **33**, 135–146.
57 D. Drouin, A. Réal Couture, D. Joly, N. Poirier-Demers and H. Demers, monte CArlo SImulation of electroN trajectory in sOlids (CASINO) ver. 3.3.0.4, http://www.gel.usherbrooke.ca/casino/.

A new composite sample preparation method for high contrast cross-sectional SEM imaging.

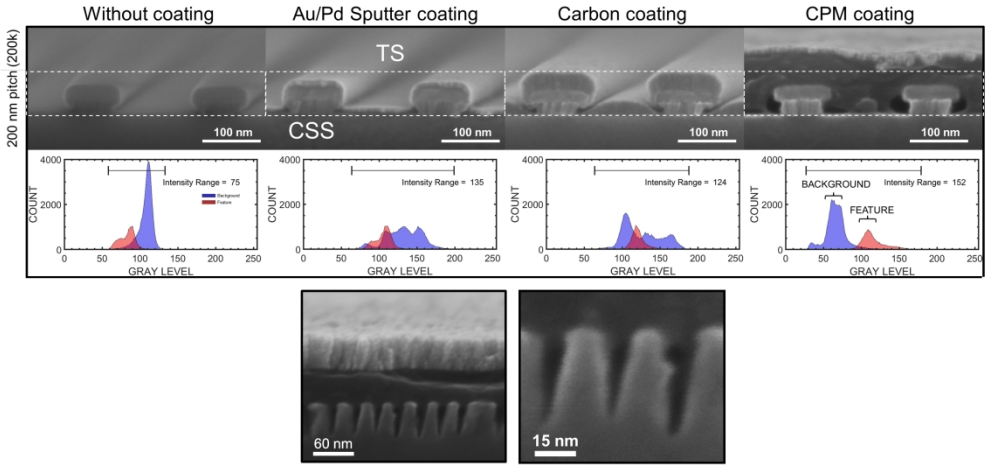

609x289mm (128 x 128 DPI)